Progress In Electromagnetics Research, Vol. 111, 43–70, 2011

A NOVEL SPHERICAL-WAVE THREE-DIMENSIONAL IMAGING ALGORITHM FOR MICROWAVE CYLINDRICAL SCANNING GEOMETRIES

W. X. Tan, W. Hong, Y. P. Wang, and Y. R. Wu

The National Key Laboratory of Microwave Imaging Technology
Institute of Electronics, Chinese Academy of Sciences
Beijing 100190, China

Abstract—With the increasing threat of terrorism in recent years, the detection of concealed weapons, plastic bombs and other contraband at secure locations attracts more and more countries' attention all over the world. Three-dimensional (3D) microwave imaging surveillance systems, allowing for acquisition of full 3D microwave images of human body, have been developed for security applications. In this paper, we firstly propose a 3D imaging algorithm which not only accounts for the free space propagation losses and wavefront curvature but also avoids 3D interpolation in the 3D wavenumber domain without suffering from any approximations and truncation errors. Then, the sampling constraints and the resolution issues associated with proper and alias-free implementation of the 3D reconstruction are analyzed. Finally, the focusing capabilities of our proposed imaging algorithm are investigated and verified by means of numerical simulations as well as theoretical analysis, and an approach for better displaying projected images is examined.

1. INTRODUCTION

In order to combat terrorism, various kinds of techniques for better security monitoring in airports or other public places have been developed for the detection of concealed weapon. The conventional metal detectors have a number of shortcomings in detecting concealed objects composed of plastic, wood, ceramic or other materials [1–7]. Microwave possesses a unique property of passing transparently through materials such as common clothing or packing. This

Received 3 October 2010, Accepted 11 November 2010, Scheduled 29 November 2010
Corresponding author: Weixian Tan (wxtan@mail.ie.ac.cn).

property provides potential to identify hidden weapons or contraband underneath a person's clothing with the help of high resolution images. In the beginning of this century, a holographic microwave imaging system employing a linear transceiver array was designed and tested [1]. Using non-ionizing radiation with low emitted power and posing no health concerns for operators and objects [1–7], the system has the capability to map the microwave reflectivity of an entire human body in 3D space and provides the base for detection, identification and further automatic recognition.

The holographic microwave imaging system operates by gathering the amplitude and phase of a wavefront scattered from a target, and reconstructs the image based on the theory of wavefront reconstruction. Range Migration Algorithm (RMA), as one kind of the holographic imaging algorithms, was developed by several authors [8–10]. The imaging system prototype for human body was originally designed with a planar scanning geometry, and the 3D Range Migration Algorithm (3D RMA) [1, 3, 10, 11] based on the planar synthetic aperture was utilized to process the data acquired over a wide frequency bandwidth. Several years later, in order to further perform full-body security screening and monitor a person from all sides without inconveniencing him, the system was improved by using a cylindrical scanning geometry, and an imaging algorithm was proposed by Sheen [2, 3]. Soumekh developed a 3D wavenumber domain algorithm for the cylindrical aperture based on the slant-range plane algorithm [10]. Contemporaneously, the 3D RMA was extended for the cylindrical aperture by expanding the 3D scalar Helmholtz equation into a sum of cylindrical harmonics and backpropagating the backscatter data to the planar aperture [11]. Recently, the development of microwave imaging systems providing 3D capability has become a field of intensive research and has been reported by several authors [12–24]. For example, an approach to detect concealed objects has been suggested, e.g., Bertl et al. [14] used interferometric Synthetic Aperture Radar (SAR) technique for imaging. However, the interferometric SAR technique is not a very good choice for 3D imaging, since it can not obtain the 3D spatial frequency space of target area with the Nyquist sampling intervals.

The algorithms mentioned above are generally used without considering the losses due to the free space propagation. When the distance between antennas and illuminated targets varies greatly under near-field conditions, the existing algorithms will degrade the quality of resulting images. More specifically, an accurate 3D interpolation [14] should be performed in the 3D wavenumber domain not only for planar but also for cylindrical scanning geometries [1–4, 11]. The

method in [2, 3] divided the whole cylindrical aperture into smaller sub-apertures and processes the received echoed signals within these sub-apertures independently, which limited the angular extent of the synthetic aperture to a span of 90°.

Fortuny [11] designed a focusing operator taking into account the free space propagation losses and obtained high quality image with an interpolation-free algorithm. However, this algorithm is based on space-variant matched filtering and only suited for the case of spherical synthetic aperture. Moreover, it is computationally costly and difficult for real time inspection of concealed weapons in practice.

In this paper, we present the formulation of a new 3D imaging algorithm, which compensates for the free space propagation losses and the wavefront curvature under near-field condition. The proposed algorithm has the advantages of low implementation complexity, not requiring any interpolation in the 3D wavenumber domain, and forming a cylindrical frame at each radius. It is noted that the above-mentioned microwave imaging systems and algorithms rely on the SAR principle [10] and they are developed in the field of linearized inverse scattering. Also the systems can be developed for breast tumor detection application in a low frequency situation (e.g., $< 3\,\mathrm{GHz}$) [25]. However, the multiple scattering phenomenon inside the object is highly non-linear, and the image formation is to solve an ill-posed non-linear inverse problem [26–29], which is not taken into account in the paper.

The structure of the paper is organized as follows. Section 2 presents the cylindrical scanning geometry, signal model, the formulation of the proposed algorithm, the algorithm implementation, the required sampling criteria and the resulting 3D resolutions. Section 3 assesses the performance of this algorithm by means of two numerical simulations and theoretical analysis, and discusses an approach to improve the quality of the focused images. Finally, the conclusions of this paper are provided in Section 4.

2. SPHERICAL-WAVE THREE-DIMENSIONAL IMAGERY RECONSTRUCTION

This section is split into three subsections. First, the algorithm which is free of 3D interpolation in the wavenumber domain with a cylindrical scanning geometry is addressed. Then, the computational procedure of this algorithm is described. Finally, the sampling criteria and the resulting resolutions which take into account the scattering angular extent of the targets are investigated with the cylindrical synthetic aperture.

2.1. Spherical-wave Imaging Algorithm

The human body imaging with a cylindrical scanning geometry is shown in Fig. 1. A stepped frequency (or frequency modulated) continuous wave (CW) signal with bandwidth B is radiated and received. An array of Transmit/Receive (Tx/Rx) antennas spans the vertical length of aperture $\overrightarrow{AB}$ for fast scanning, and the corresponding equivalent sample points in the z-axis is acquired. Considering the equivalent sample point in the z-axis is located at $P(x', y', z')$ in Cartesian coordinates, the corresponding cylindrical coordinate is $P(\rho'_0, \phi', z')$. The antenna array rotates on the surface of a cylinder with radius ρ'_0 and forms a cylindrical aperture $\widehat{ACD}$ which completely surrounds the target. The axis of the synthetic aperture coincides with the z-axis. Since the antennas are located within the near-field region of the object [11], the distortion caused by a spherical wavefront and free space propagation losses should not be ignored. Denote the backscattered field function as $E(K_\omega, \phi', z')$, which is a function of four parameters: the working frequency wavenumber K_ω of the CW signal, the radius ρ, the azimuth angle position ϕ and height position z of the illuminated objects. Suppose that the 3D complex reflectivity functions of the distributed targets in Cartesian and cylindrical coordinates are $I(x, y, z)$ and $I(\rho, \phi, z)$, respectively. In this case, the measured echoes from a given point scatterer located

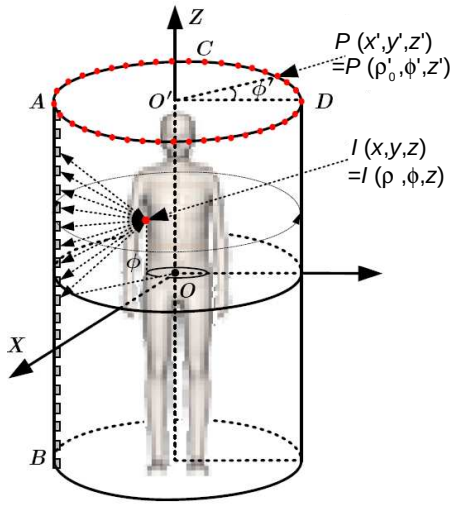

Figure 1. Cylindrical imaging geometries with human body.

at (ρ, ϕ, z) under near-field condition can be written as

$$E_I\left(K_\omega, \phi', z'\right) = I\left(\rho, \phi, z\right) \frac{\exp\left(-j2K_\omega R\right)}{R^2} \tag{1}$$

where K_ω is the frequency wavenumber, and is related to instantaneous frequency f and the speed of light C via $K_\omega = 2\pi f/C$. $K_\omega \in [K_{\omega\,\min}, K_{\omega\,\max}]$, where $K_{\omega\,\min}$ and $K_{\omega\,\max}$ denote the wavenumbers at the minimum and maximum frequencies, respectively. R is the distance between the target (ρ, ϕ, z) and the transceiver antenna (ρ_0', ϕ', z'); that is,

$$\begin{aligned} R &= \sqrt{\left(x - x'\right)^2 + \left(y - y'\right)^2 + \left(z - z'\right)^2} \\ &= \sqrt{\rho'^2 + \rho^2 - 2\rho'\rho\cos\left(\phi - \phi'\right) + \left(z - z'\right)^2} \end{aligned} \tag{2}$$

Consequently, the backscattered fields $E\left(K_\omega, \phi', z'\right)$ of illuminated target area could be measured over a range of frequency, azimuth aspect angles and elevation positions of the antenna (ϕ', z'). When ignoring the interaction between scatterers, the response measured at transceiver position (ρ_0', ϕ', z') at instantaneous frequency wavenumber K_ω has the following form:

$$\begin{aligned} E\left(K_\omega, \phi', z'\right) &= \iiint_{\mathbf{V}} E_I\left(K_\omega, \phi', z'\right) d\mathbf{r} \\ &= \iiint_{\mathbf{V}} I\left(\rho, \phi, z\right) \frac{\exp\left(-j2K_\omega R\right)}{R^2} d\mathbf{r} \end{aligned} \tag{3}$$

where $\mathbf{V}$ and $\mathbf{r}$ denote the illuminated area and the vector position of the targets, respectively. Thus, $d\mathbf{r} = dxdydz = \rho d\rho d\phi dz$. $|\phi - \phi'| \leq \phi_A/2$, where ϕ_A represents the azimuth angular span in which the backscattering of the target is homogeneous and isotropic. $|z - z'| \leq L_Z/2$, where L_Z is the elevation aperture length and determined by $-3\,\mathrm{dB}$ beam width ϕ_Z in elevation. It should be emphasized that the resolutions in azimuth and elevation are determined by ϕ_A and ϕ_Z, respectively. This will be derived in the next section in detailed form. With the signal model in (3), the free space propagation losses and the exact spherical-wave phase history are both investigated by a quadratic term in the amplitude and the exponential function, respectively.

The signal model based on (1) and (3) indicates that the amplitude of the received echoes from different targets is proportional to R^2. When ignoring the disturbance of this term, the quality of the image focusing would be degraded [11]. Unfortunately, they are difficult to be directly removed in the frequency domain. When a slant-range inverse Fourier transform with respect to K_ω is performed on $E\left(K_\omega, \phi', z'\right)$, the amplitude of the impulse response is also proportional to R^2 in

the slant-range domain. Hence, we compensate for the free space propagation losses through multiplying an amplitude function R^2 in the slant-range domain, followed by slant-range Fourier transform for all pairs (ϕ', z') in (3); that is

$$\begin{aligned} E_R\left(K_\omega, \phi', z'\right) &= \int_R \int_{K_\omega} \left\{E\left(K_\omega, \phi', z'\right) \exp\left(jK_\omega R\right) dK_\omega\right\} \\ &\quad \times R^2 \exp\left(-jK_\omega R\right) dR \\ &= \iiint_{\mathbf{V}} I\left(\rho, \phi, z\right) \exp\left(-j2K_\omega R\right) d\mathbf{r} \end{aligned} \tag{4}$$

In practice situations, the direct coupling wave is always present in the received signal due to quasi monostatic measurements. In addition, undesired echoes reflected from the targets beyond the region of interest are always received, too. Fortunately, range gating can be used to remove the antenna direct coupling and the undesired targets in the slant-range domain in (4) before Fourier transform. It uses a windowing function to filter the slant-range domain signal in (4) and only selects the signal of interest. To further reduce the computational load and data volume, one could subsample $E_R\left(K_\omega, \phi', z'\right)$ in the K_ω domain on the basis of no aliasing. Then, the useful signal reflected from the human body could be picked up for further processing at the subsampled set.

Since the measurement is performed at a fixed cylindrical radius ρ_0', when determining the 3D microwave reflectivity map associated with a person, we use an integral resembling inverse transform of (4) with respect to K_ω, ϕ' and z' described in the Appendix; this yields

$$\begin{aligned} I\left(\rho, \phi, z\right) &= \int_{z'} \int_{\phi'} \int_{K_\omega} E_R\left(K_\omega, \phi', z'\right) \\ &\quad \times \exp\left(+j2K_\omega R\right) K_\omega dK_\omega d\phi' dz' \end{aligned} \tag{5}$$

It is seen that the expected image could not be directly represented as a function of x', y' and z' in (5) for the cylindrical scanning geometry. However, the integral in (5) could not be formulated in the form of the Fourier transform. Therefore, the image reconstruction is much more complicated than the case in [1]. According to our knowledge, all the existing algorithms need high accurate interpolation in wavenumber domain. The following discussions and derivations are based on the model in (5).

As for the solution to (5), both Sheen [2, 3] and Soumehk [10] decomposed the spherical-wave into plane-wave components via two-dimensional (2D) Fourier transform. The decomposition is performed in x-y plane, so ϕ is limited in $(-90^\circ, +90^\circ)$ [2, 3, 10]. Thus, only

a sub-aperture frame with a maximum angular span of 180° could be reconstructed at a time. In this section, we do not perform the decomposition in the ϕ domain but calculate the Fourier expansion for spherical-wave signal $\exp(+j2K_\omega R)$ in (5) with respect to elevation variable z as follows:

$$\begin{aligned}
&\exp\left(+j2K_\omega\sqrt{\rho'^2+\rho^2-2\rho'\rho\cos(\phi-\phi')+(z-z')^2}\right)\\
&=\int\exp\left\{j\sqrt{4K_\omega^2-K_z^2}\sqrt{\rho'^2+\rho^2-2\rho'\rho\cos(\phi-\phi')}\right\}\\
&\quad\times\exp\left\{jK_z\left(z-z'\right)\right\}dK_z
\end{aligned}\tag{6}$$

Substituting the Fourier expansion in (6) into (5) and interchanging the order of the integrals over K_z and ϕ', the solution to (6) can be expressed as

$$\begin{aligned}
I(\rho,\phi,z) &= \int_{K_z}\int_{K_\omega}\left\{\int_{\phi'}E_R\left(K_\omega,\phi',K_z\right)\right.\\
&\quad\left.\times F\left(K_\omega,\phi-\phi',K_z\right)d\phi\right\}dK_\omega\exp\left[jK_zz\right]dK_z
\end{aligned}\tag{7}$$

wherein

$$E_R\left(K_\omega,\phi',K_z\right)=\int_{z'}E_R\left(K_\omega,\phi',z'\right)\exp\left(-jK_zz'\right)dz'.\tag{8}$$

and

$$F\left(K_\omega,\phi',K_z\right)=\exp\left[j\sqrt{4K_\omega^2-K_z^2}\sqrt{\rho'^2+\rho^2-2\rho'\rho\cos\phi'}\right]K_\omega\tag{9}$$

where $|\phi'|\le\phi_A/2$.

Because K_ω is not mutually orthogonal to K_ϕ and K_z, the 3D spectrum $I(K_x,K_y,K_z)$ should be acquired through 3D high accurate interpolation, as discussed in [2, 10, 11]. In fact, we are usually interested in forming the image at the given radius bins ρ's rather than all the available area. So it is feasible to first obtain the image frame at radius ρ by setting the proper matched function in (9). Moreover, the values of its parameters (the frequency $K_\omega=2\pi f/C$, the angle sampling interval $\Delta\phi$, the elevation sampling interval Δz, the radius ρ' of the cylinder, etc.) are always known for a given people screening system. Therefore, we can obtain the image at radius ρ through defining the radius ρ iteratively and using $F(K_\omega,\phi',K_z)$. Now, we refer to $F(K_\omega,\phi',K_z)$ in (9) as the cylinder focusing function accordingly.

As shown in the above Equations (8) and (9), $E_R(K_\omega,\phi',K_z)$ is a function of ϕ', and $F(K_\omega,\phi-\phi',K_z)$ is a function of $(\phi-\phi')$.

Evidently, the terms inside the { } in (7) represents a convolution integral in the ϕ domain; that is

$$I(\rho,\phi,z) = \int_{K_z}\int_{K_\omega}\Big\{ E_R\left(K_\omega,\phi',K_z\right) \otimes F\left(K_\omega,\phi',K_z\right)\Big\} dK_\omega \exp\left[jK_z z\right] dK_z \tag{10}$$

where $\otimes$ denotes convolution in the azimuth ϕ' domain, and the convolution can be computed in the Fourier domain for efficiency; that is, it can be calculated with a complex product in wavenumber K_ϕ domain and one-dimensional (1D) inverse Fourier transform with respect to K_ϕ via the following formula:

$$E_R\left(K_\omega,\phi',K_z\right) \otimes F\left(K_\omega,\phi',K_z\right) = \int_{K_\phi} E_\rho\left(\rho,K_\omega,K_\phi,K_z\right)\exp\left[jK_\phi\phi\right] dK_\phi \tag{11}$$

and

$$E_\rho\left(\rho,K_\omega,K_\phi,K_z\right) = \mathrm{FT}_\phi\left[E_R\left(K_\omega,\phi,K_z\right)\right] \times \mathrm{FT}_\phi\left[F\left(K_\omega,\phi,K_z\right)\right] \tag{12}$$

where FT_ϕ denotes the Fourier transform with respect to ϕ.

Thus, by substituting (11) and (12) into (7), interchanging the integral order again, a 3D image could be reconstructed via the following:

$$I(\rho,\phi,z) = \int_{K_z}\int_{K_\phi}\left\{\int_{K_\omega} E_\rho\left(\rho,K_\omega,K_\phi,K_z\right) dK_\omega\right\} \times \exp\left[jK_\phi\phi\right] dK_\phi \exp\left[jK_z z\right] dK_z \tag{13}$$

The above 1D integral with respect to K_ω can be converted into a summation over the available discrete values of K_ω instead of spatial frequency interpolation from K_ω to (K_x, K_y, K_z) domain. In its discrete form of (13), the target function can be formed via

$$I(\rho,\phi,z) = \left\{\mathrm{IFT}_{K_\phi,K_z}\left[\sum_{K_\omega} E_\rho\left(\rho,K_\omega,K_\phi,K_z\right)\Delta K_\omega\right]\right\} \tag{14}$$

where $\mathrm{IFT}_{K_\phi,K_z}$ indicates the inverse Fourier transform with respect to K_z and K_ϕ. Usually, the computation can be efficiently implemented via Fast Fourier Transform (FFT) and Inverse Fast Fourier Transform (IFFT) codes. With the coherent summation with respect to K_ω inside [ ], we can obtain the reflectivity spectrum of the cylinder's surface at fixed radius ρ. Subsequently, we can obtain the reflectivity distribution

on the cylinder of radius ρ by simply applying 2D IFT with respect to spatial frequency K_z and angular frequency K_ϕ.

Repeating the operations involved from (12) to (14), the target function at the individual radius bins ρ's could be recovered. Then, the resulting image on the cylinder can be assembled to form the complete 3D reflectivity image $I(\rho, \phi, z)$. If the backscattering of the targets is not homogenous within 360°, we can obtain the images of high quality with the focusing function $F(K_\omega, \phi - \phi', K_z)$ through adjusting proper spans of K_ϕ which is determined by the azimuth support of the target. It should be noted that the algorithm is suitable for sub-aperture image formation if necessary.

In above mathematical derivations, we have not performed any interpolations in wavenumber domains, namely, our algorithm is free of interpolation, and thus it does not suffer from the errors due to the truncation of interpolation kernel. Also we have not made near-field Fresnel approximation or far-field approximation. Therefore, the 3D image of the human body could be reconstructed accurately. Especially, as the focusing functions $F(K_\omega, \phi', K_z)$ at different radius ρ in (9) are independent with each other, they can be calculated and stored on disk in advance. This enables the use of parallel implementation of the algorithm, so we can obtain the cylindrical frame of different radius simultaneously. If we would like to display the image, measure the head-to-toe body (waistline, circumference, etc.) in Cartesian coordinates system and calculate physical measurements for developing better-fitting clothing, a geometric transformation between the cylindrical coordinates and Cartesian coordinates system can be applied via:

$$\begin{cases} x = \rho \cos \phi \\ y = \rho \sin \phi \\ z = z \end{cases} \tag{15}$$

This geometric transform is performed in the image domain of interest. So, it does not need for special treatment for high phase-preserving accuracy, and the polynomial interpolation is usually enough.

2.2. Reconstruction Procedure

This section deals with the practical implementation of the spherical-wave 3D imaging algorithm. The whole procedure to reconstruct a 3D reflectivity image of a person is summarized in the flowchart in Fig. 2, and the approach may be split into the following steps:

Step 1: Perform the Inverse Fourier Transform (IFT) of the measured echoes (frequency domain data) with respect to K_ω. Compensate for the free space propagation losses, and reduce the

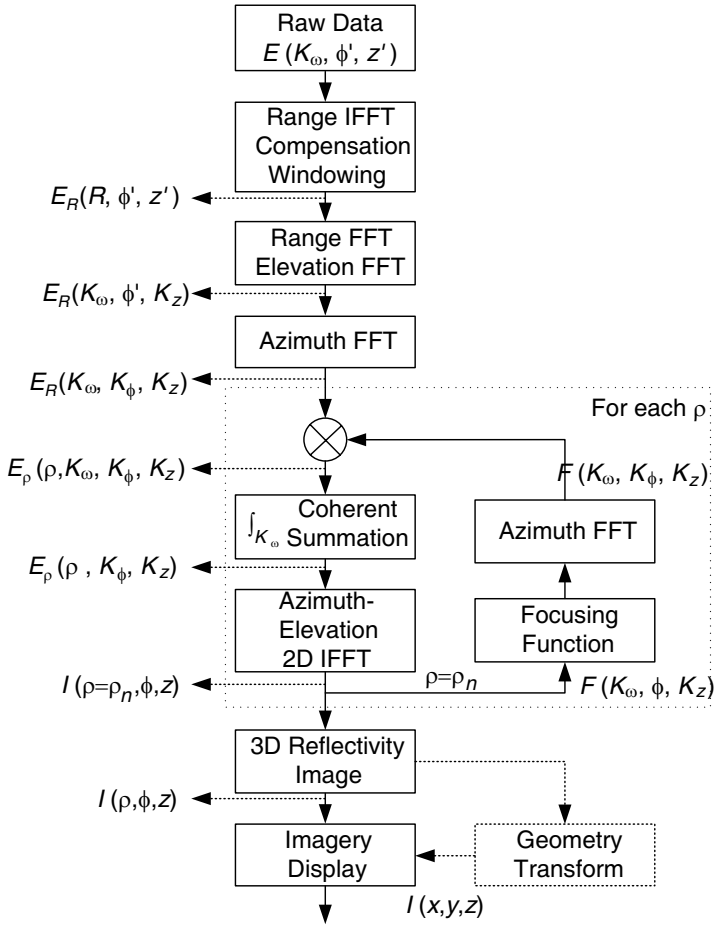

Figure 2. Block diagram representation of the spherical-wave 3D imaging algorithm.

coupling and undesired targets through windowing the signal in the slant-range domain.

Step 2: Obtain the 2D Fourier Transform (FT) of $E_R(R, \phi', z')$ acquired in step 1 with respect to R and z'.

Step 3: Calculate the FT of the signal $E_R(K_\omega, \phi', K_z)$ with respect to the azimuth angle ϕ' for each frequency wavenumber K_ω and each elevation spatial frequency K_z.

Step 4: Evaluate the FT of the focusing function $F(K_\omega, \phi, K_z)$ with respect to ϕ at a desired radius $\rho = \rho_n$, the elevation spatial frequency K_z and the frequency wavenumber K_ω. To alleviate the

computational load, we can also use the results stored on disk in advance.

Step 5: Take the complex product of the results from Step 3 and Step 4 in the azimuth wavenumber domain. Sum the resulting product over the available frequencies K_ω to yield the marginal FT of the target function at the fixed radius ρ_n.

Step 6: Perform the 2D IFT of the summation with respect to K_ϕ and K_z to obtain the reflectivity image $I(x, y, z)$ of the cylinder at the fixed radius ρ_n.

Step 7: Repeat Steps 4 to 6 for all the available radii ρ's, and then assemble the results together to form a 3D image of the human body. The main merit of this step is in its rapid implementation by employing parallel processing, as indicated in the rectangle with dotted lines in Fig. 2.

Step 8: Display the 3D image projected onto the cylinder, also the image could be transformed into the Cartesian coordinates system if necessary, as shown in the rectangle with dashed lines in Fig. 2.

This algorithm has two merits. First, it does not require any complex 3D interpolation in the 3D wavenumber domain. Second, a multiprocessor computer can be programmed to form different frames at the fixed radius in a parallel form; this would greatly reduce the computational time for image reconstruction.

2.3. Sampling Criteria and Resolutions

According to the Nyquist sampling criterion, the sampling intervals in the ϕ', z' and K_ω directions depend on the extent of the volume occupied in the spatial frequency domain synthesized with motion along cylindrical surface. The sampling criterion under near-field condition using the cylindrical scanning geometry has been given by Fortuny [11], but the field of view is confined to a small specific angle. For human body imaging, the field of view is sometimes expected to reach as large as 360°, and the existing sampling constraints for acquiring the echoed data will cause severe aliasing problem associated with the image reconstruction. Now, we continue with discussion and analysis including the sampling constraints and resolving capabilities under the cylindrical scanning geometry condition.

As for the direction of propagation, the frequency domain support band of the transmitted signal is determined by

$$\Omega_{K_\omega} = [2K_{\omega\,\min}, 2K_{\omega\,\max}] \tag{16}$$

where $K_{\omega\,\min}$ and $K_{\omega\,\max}$ are the wavenumbers at the minimum and maximum frequencies, respectively. To sample the echoed signal

without aliasing, the following Nyquist sampling constraint should be satisfied,

$$\frac{R_{\max}}{\frac{K_{\omega\max}-K_{\omega\min}}{\Delta K_\omega}} \leq \frac{2\pi}{2\left[K_{\omega\max}-K_{\omega\min}\right]}$$
$$\Rightarrow \Delta K_\omega \leq \frac{\pi}{R_{\max}} \Rightarrow \Delta f \leq \frac{C}{2R_{\max}}, \tag{17}$$

where Δf is the frequency sampling interval, $R_{\max}$ denotes the maximum observed distance within the antenna beam pattern.

As for the elevation direction, the samples are realized with an antenna array. However, the whole bandwidth is imposed by the size of the individual antenna. The wavenumber support band $\Omega_{K_{z'}}$ is

$$\Omega_{K_{z'}} = \left[-2K_\omega \sin\left(\frac{\phi_Z}{2}\right), 2K_\omega \sin\left(\frac{\phi_Z}{2}\right)\right] \tag{18}$$

Based on the above wavenumber support band, the Nyquist sampling spacing $\Delta z'$ in the z' domain for gathering echoed signal must satisfy the following inequality:

$$\Delta z' \leq \frac{2\pi}{4K_\omega \sin\left(\frac{\phi_Z}{2}\right)} \Rightarrow \Delta z' \leq \frac{2\pi}{4K_{\omega\max} \sin\left(\frac{\phi_Z}{2}\right)} = \frac{\lambda_{\min}}{4\sin\left(\frac{\phi_Z}{2}\right)} \tag{19}$$

where $\lambda_{\min}$ is the smallest wavelength at the highest frequency $K_{\omega\max}$. The worst-case scenario corresponds to the case of $\phi_Z = 180^\circ$ for which the Nyquist sampling spacing in the z' domain is

$$\Delta z' \leq \frac{\lambda_{\min}}{4} \tag{20}$$

As for the azimuth direction, we can approximate the instantaneous azimuth angular frequency of the signal $E_R\left(K_\omega, \rho'_0,\ \phi', K_z\right)$ obtained in Step 2 via

$$K_{\phi'} = \frac{\partial}{\partial \phi'}\left\{\arg\left[E_R\left(K_\omega, \rho'_0,\ \phi', K_z\right)\right]\right\}$$
$$\approx \frac{\rho\rho' \sin\left(\phi-\phi'\right)\sqrt{4K_\omega^2 - K_z^2}}{\sqrt{\rho'^2+\rho^2-2\rho\rho'\cos\left(\phi-\phi'\right)}} \tag{21}$$

Considering the earlier assumption that the backscattering of a point target is homogeneous and isotropic in spans of ϕ_A, and $\phi_A \in [0^\circ, 360^\circ]$, the azimuth spectral support can be expressed as:

$$\Omega_{K_{\phi'}} = \left[K_{\phi'}\big|_{\phi'=K_{\phi'\min}}, K_{\phi'}\big|_{\phi'=K_{\phi'\max}}\right] \tag{22}$$

where

$$\phi'_{K_{\phi'}\max} = \begin{cases} \phi - \gamma, & \phi_A \in [2\gamma, 2\pi] \\ \phi - \phi_A/2, & \phi_A \in [0, 2\gamma] \end{cases} \tag{23}$$

$$\phi'_{K_{\phi'}\min} = \begin{cases} \phi + \gamma, & \phi_A \in [2\gamma, 2\pi] \\ \phi + \phi_A/2, & \phi_A \in [0, 2\gamma] \end{cases} \tag{24}$$

and $\gamma = \arccos(\rho/\rho'_0)$. As the observed area $\rho = \rho_{\max}$ is always smaller than the radius ρ'_0 of the cylinder, γ is limited to the interval $(0°, 90°)$. Then, the Nyquist sampling spacing in the ϕ' domain should satisfy

$$\Delta\phi' \le \frac{2\pi}{B_{\phi'}\big|_{\rho=\rho_{\max}}} = \begin{cases} \frac{2\pi}{2\rho\sqrt{4K_\omega^2 - K_z^2}}, & \phi_A \in [2\gamma, 2\pi] \\ \frac{\pi\sqrt{\rho^2 + \rho'^2_0 - 2\rho\rho'_0\cos(\phi_A/2)}}{\rho'_0\rho\sin(\phi_A/2)\sqrt{4K_\omega^2 - K_z^2}}, & \phi_A \in [0, 2\gamma] \end{cases} \tag{25}$$

To choose an azimuth angular sample spacing suitable for all the available K_ω and ϕ_A, the above constraint must be satisfied for the worst case, that is, the smallest wavelength $\lambda_{\min}$ and the isotropic backscattering angle ϕ_A ($\phi_A > 2\gamma$); this yields

$$\Delta\phi' \le \frac{2\pi}{2\rho\sqrt{4K_\omega^2 - K_z^2}} \Rightarrow \Delta\phi' \le \frac{\pi}{2\rho_{\max}K_{\omega\max}} = \frac{\lambda_{\min}}{4\rho_{\max}} \tag{26}$$

The above inequality indicates that the azimuth sampling interval is mainly determined by $\lambda/4$ and the scanning radius, which is usually enough for full-body data acquisition and alias-free reconstruction.

The wavenumber support band and the sampling constraints discussed above rely on the dimensions of the volume occupied in the 3D wavenumber domain. Therefore, the spatial resolutions of the resulting 3D reflectivity image $I(\rho, \phi, z)$ are dictated by the signal bandwidth, the center frequency, the extent of the synthetic aperture and the homogeneous properties of the targets. The achieved -3 dB resolutions in polar-radius ρ, azimuth ϕ and height z can be approximated as:

$$\delta_\rho \approx \frac{0.886\pi}{K_{\omega\max} - K_{\omega\min}} \tag{27}$$

$$\delta_\phi \approx \begin{cases} \frac{0.886\lambda_c}{4}, & \phi_A \in [2\gamma, 2\pi] \\ \frac{0.886\lambda_c}{4\sin(\phi_A/2)}\beta, & \phi_A \in [0, 2\gamma] \end{cases} \tag{28}$$

$$\delta_z \approx \frac{0.886\lambda_c}{4\sin(\phi_Z/2)} \tag{29}$$

with $\beta = \sqrt{\cos^2\gamma + 1 - 2\cos\gamma\cos(\phi_A/2)}$, $\gamma = \arccos(\rho/\rho'_0)$ and λ_c is the wavelength at the center frequency f_c. Note that all the units of δ_ρ,

δ_ϕ and δ_z are meters. In practice, due to the side lobes of the radiation patterns, the final resolutions are usually slightly poorer than above theoretical resolutions.

In summary, as for the human body imaging with cylindrical scanning geometry, the sampling intervals in the measurement are fixed according to the upper bounds in (17), (19) and (25). The corresponding spatial resolutions of resulting images are determined by (27), (28) and (29).

3. SIMULATION RESULTS

In this section, we present two numerical simulation examples based on cylindrical configuration to illustrate the performance of our algorithm. The parameters used in the simulation experiments are listed in Table 1. For the sake of simplicity, the losses due to the antenna pattern are not considered here.

In the first numerical simulation, to illustrate the capability of reconstructing the image on the cylinder of particular radius with the proposed algorithm, 18×17 point scatterers are evenly distributed on a cylinder of radius $\rho = 0.20\,\mathrm{m}$ with spacings 20° and $0.10\,\mathrm{m}$ in azimuth and elevation, respectively. As shown in Fig. 3(a), a sketch of point targets in the 3D space is depicted, and the projection of them onto the cylinder of radius $\rho = 0.20\,\mathrm{m}$ is also shown in Fig. 3(b). All the scatters have the same radar cross section, and all the backscattering angles ϕ_A of the model in azimuth are approximated as 30°. That is

Table 1. Measurement parameters used in the simulations.

Parameter	Value
Frequency Range (GHz)	$35.000 \sim 40.000$
Radius of Cylindrical Aperture (m)	1.500
Frequency Sampling Interval (MHz)	50.000
Azimuth Scattering Angle ϕ_A ($^\circ$)	30.000
Azimuth Sampling Interval ($^\circ$)	0.358
Elevation Beam Width ϕ_Z ($^\circ$)	30.000
Elevation Sampling Interval (cm)	0.600
Range Direction Resolution (cm)	2.658
Azimuth Direction Resolution (cm)	0.597
Elevation Direction Resolution (cm)	0.685

to say, although the targets are illuminated within 360°, the echoed signal reflected from each target is generated with an angular span of ±15°. Then, the TX/RX antenna array synthesizes a cylindrical aperture of radius $\rho_0' = 1.5\,\text{m}$ within the region $-15° \leq \phi_A \leq +15°$ and $-15° \leq \phi_Z \leq +15°$ for each point scatter. The corresponding azimuth and elevation sampling spacings are selected according to (19) and (25). The object is illuminated in the frequency range 35 to 40 GHz, sweeping 101 frequency points with a step of 50 MHz. With these parameters the expected −3 dB resolutions along the three main axes are given in the last three rows of Table 1.

The focusing function $F(K_\omega, \phi', K_z)$ is calculated with (9), and corresponding image frame on the cylinder of radius 0.20 m is formed, as shown in Fig. 4(a). Subsequently, the 3D image inside a cylinder of dimensions 0.3 m (polar-radius) ×360° (azimuth) × 1.7 m (elevation) is reconstructed with the proposed algorithm and demonstrated in Fig. 4(b). The reflectivity values as well as the position of the point targets are all in perfect agreement with the simulated model. Since the main lobe of the Point Spread Function (PSF) in polar-radius which is dominated by the bandwidth of the transmitted signal is wider than those in azimuth and elevation, the targets in the discrete image are not the ideal points. Therefore, when the image is directly projected onto the azimuth-elevation plane, the unexpected main lobes would

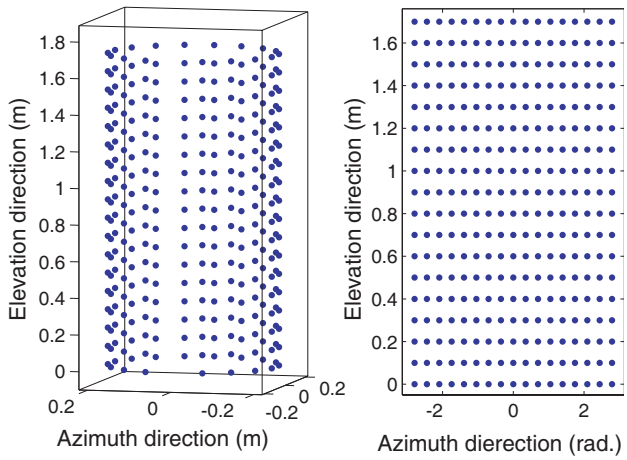

Figure 3. (a) Simulated model used in the simulation with an ensemble of 17 × 18 = 306 point targets and (b) the projection of targets onto the cylinder of radius $\rho = 0.20$ m.

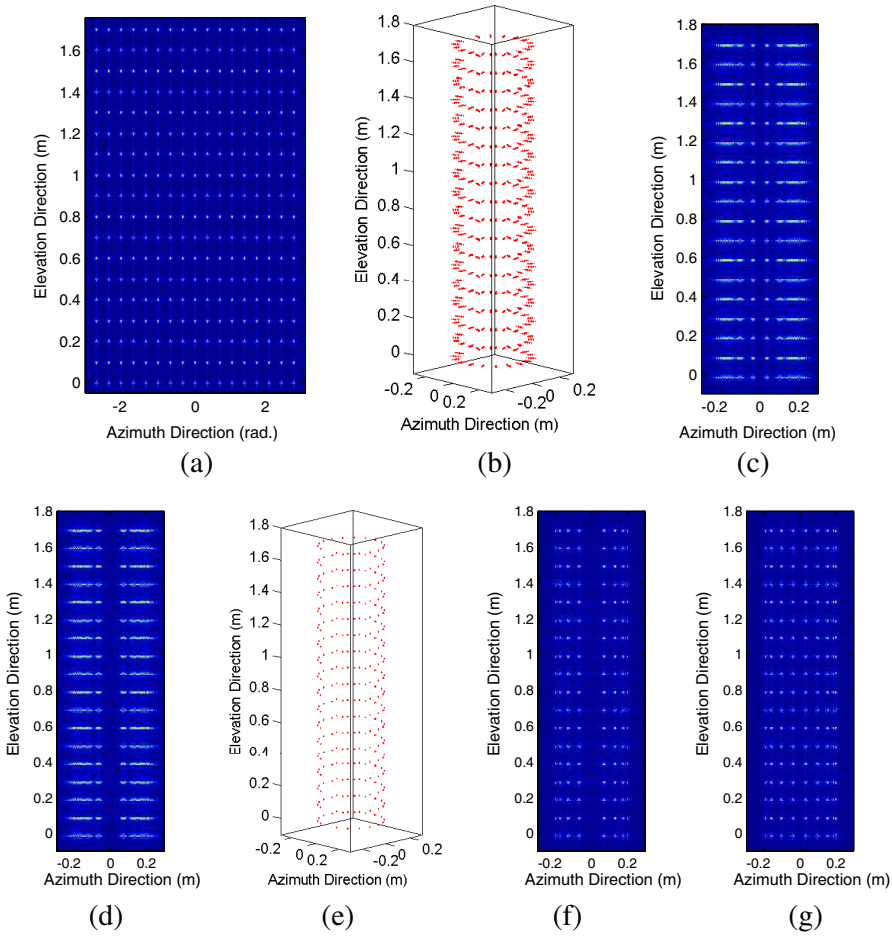

Figure 4. (a) The 2D image on the cylinder of radius 0.20 m; (b) Iso-surfaces of the 3D image processed by the proposed algorithm; (c)–(d) Direct projection of (b) onto the front and back plane; (e) Iso-surfaces of 3D image with maximum values extraction along the polar-radius direction; (f)–(g) Projection of (e) onto the front and back plane. The pixel spacings $\Delta\phi = 0.349$ rad., $\Delta z = 0.60$ cm in (a) and $\Delta x = \Delta y = 0.50$ cm, $\Delta z = 0.60$ cm in (b)–(g).

impact on the quality of the projected image, and only the targets in the middle columns could be observed clearly, as shown in Figs. 4(c)–(d).

On the one hand, as for people screening system, resolutions in azimuth and elevation are much easier achieved than that in polar-radius. Thus the main lobe of PSF in polar-radius is much wider than those in the other two directions, as shown in the upper left of Fig. 5. On the other hand, PSF of a target with cylindrical aperture is shift-varying [20], namely, the orientation of PSF varies in azimuth, as shown in Fig. 5. Therefore, when the 3D image is projected onto 2D plane directly [1], the main lobe of the PSF in polar-radius would possibly be scattered due to the shift-varying properties of PSF, as depicted in Fig. 5 (e.g., 'A' is directly projected and shown as 'C') and Figs. 4 (c)–(d).

Here, we exploit a method to improve the quality of the projected images. In practice, people can be arranged to stand in the middle of the cylinder for screening. Furthermore, the systems are not capable of penetrating human tissues but acquiring the information of body surface and concealed items. So the number of targets of interest is always less than the number of resolution cell in polar-radius. Here, we pick up these targets via extracting the maximum value of the target in polar-radius. Their absolute values should be greater than those of pixel points from a small neighborhood, and moreover, the distance between any two pixel points is larger than the width of main lobe of the impulse response. Then the 3D image can be projected not only onto spread cylinder of radius ρ, but also onto arbitrary vertical planes using the maximum values projection. This procedure is depicted in Fig. 5. Taking target 'A' as an example, we select it at first in polar-radius, pick up the maximum value (target 'B') and then project it onto the vertical plane (target 'D'). As shown in Figs. 4(e)–(g), the quality of the resulting images is greatly improved compared with Figs. 4(b)–(d).

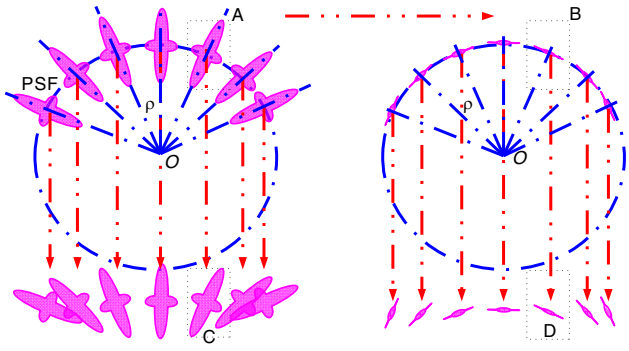

Figure 5. An approach to display the resulting 3D image.

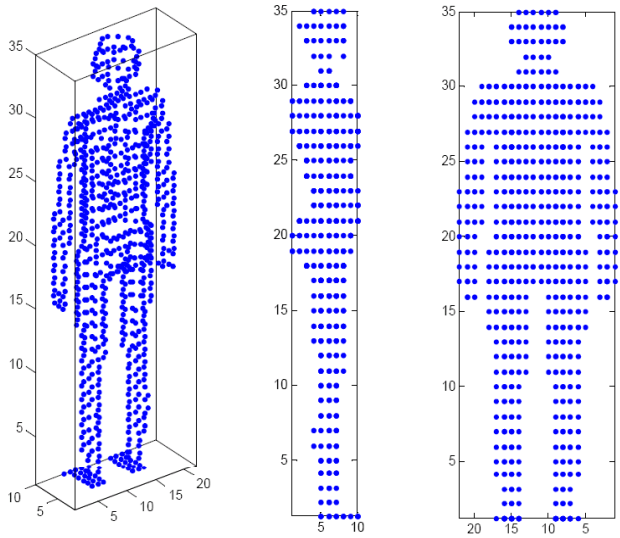

Figure 6. (b) Side view and (c) front view of (a) the human body model with an ensemble of 816 point targets.

In the second numerical simulation, a human body model consisting of 816 unit amplitude point scatters is confined within a box of dimensions 25.0 cm × 50.0 cm × 170.0 cm. Fig. 6(a) shows its sketch with pixel spacings 2.5 cm and 5.0 cm on horizontal plane and in elevation, respectively. Figs. 6(b)–(c) give the side and front views of the model, respectively. By using the same simulation parameters as in Table 1, the image reconstructed by the proposed algorithm is shown in Figs. 7(a)–(c). Then with the above-mentioned imagery representation method, the iso-surface of the 3D image and the projected images corresponding to the front and side views are shown in Figs. 7(d)–(f), respectively.

In order to demonstrate the performance of the proposed imaging algorithm, the 3D resolutions, the Peak Side Lobe Rates (PSLR) and the Integral Side Lobe Rates (ISLR) are all evaluated, as indicated in Table 2. The PSLR is the ratio between the height of the largest sidelobe A_{side} and the height of the main lobe A_{main}; that is

$$\text{PSLR} = 20\log_{10}\left\{\frac{A_{\text{side}}}{A_{\text{main}}}\right\} \tag{30}$$

The ISLR is often used to analyze the sidelobe power of PSF. Assume that the "main lobe" power is P_{main} and the total power P_{total}, the

ISLR is then

$$\mathrm{ISLR} = 10\log_{10}\left\{\frac{P_{\mathrm{total}} - P_{\mathrm{main}}}{P_{\mathrm{main}}}\right\} \tag{31}$$

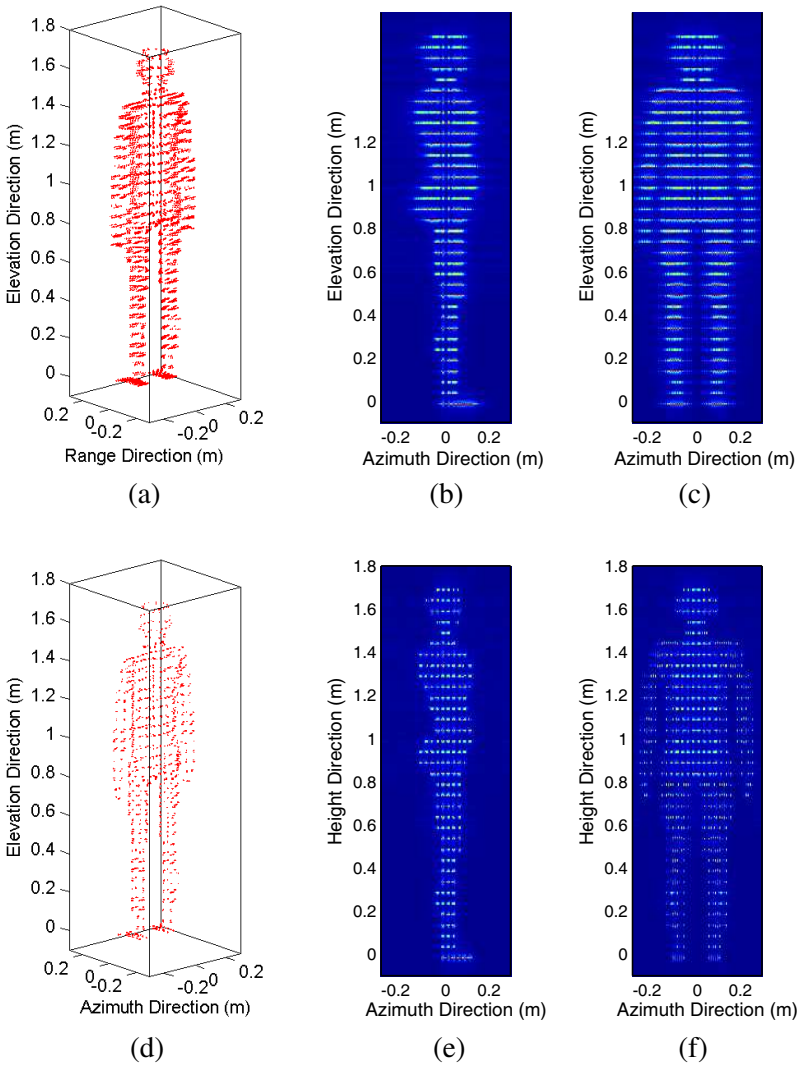

Figure 7. (a) Iso-surfaces of the 3D image processed by our algorithm in the numerical simulation with 816 point targets; (b)–(c) Direct projection of (a) onto the side and front plane; (d) Iso-surfaces of the 3D image with maximum values extraction in the polar-radius direction; (e)–(f) Projections of (d) onto the side and front plane.

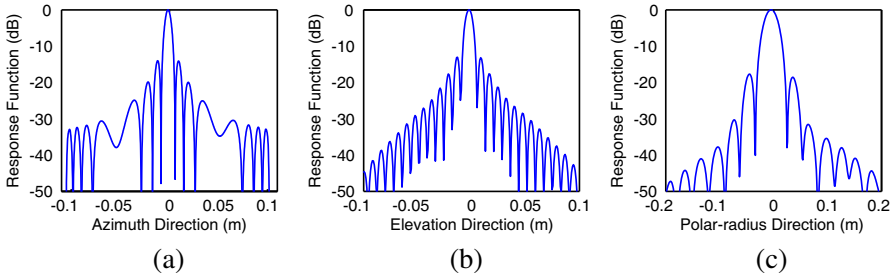

Figure 8. (a) Azimuth, (b) elevation and (c) polar-radius profiles of the 3D image of one target obtained in the simulation.

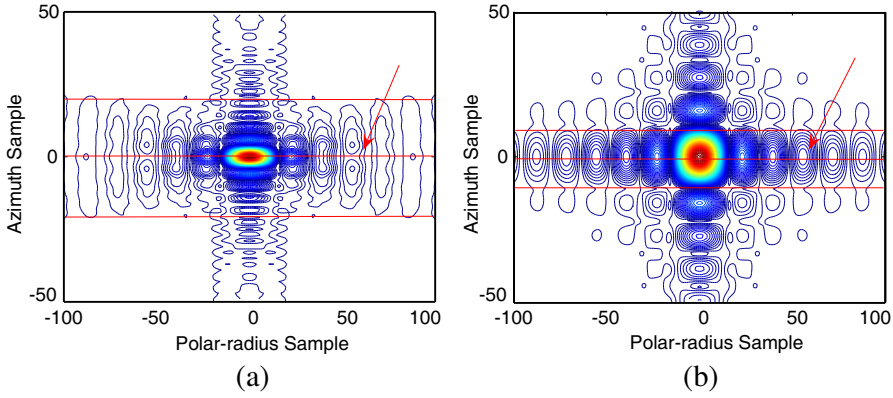

Figure 9. The scatter response for the case $\phi_A = 30°$ (a) and for the case $\phi_A = 5.5°$ (b) on the azimuth and polar-radius plane. The displayed dynamic range is 40 dB.

where the numerator is the total power of the sidelobes. Usually, the null-to-null of the PSF can be defined as the main lobe width. For a sinc function resulting from the IFT of a uniform spectrum, the typical PSLR and ISLR are about -13 dB and -10 dB, respectively.

Figure 8 shows azimuth, elevation and polar-radius profiles of a point target in Fig. 4(b) and Fig. 7(a). Note that no window is used in the reconstruction. Since the theoretical resolutions are calculated at the center frequency $f_c = 37.5$ GHz, this makes only a minor difference between the measurements and the expected ones. As we pointed out earlier, the angular extents ϕ_A and ϕ_Z exceed the spherical sector required for equal resolutions in the polar-radius, azimuth and elevation directions. The resolution in polar-radius is worse than those in the other two directions. Thus the power of the side lobes of

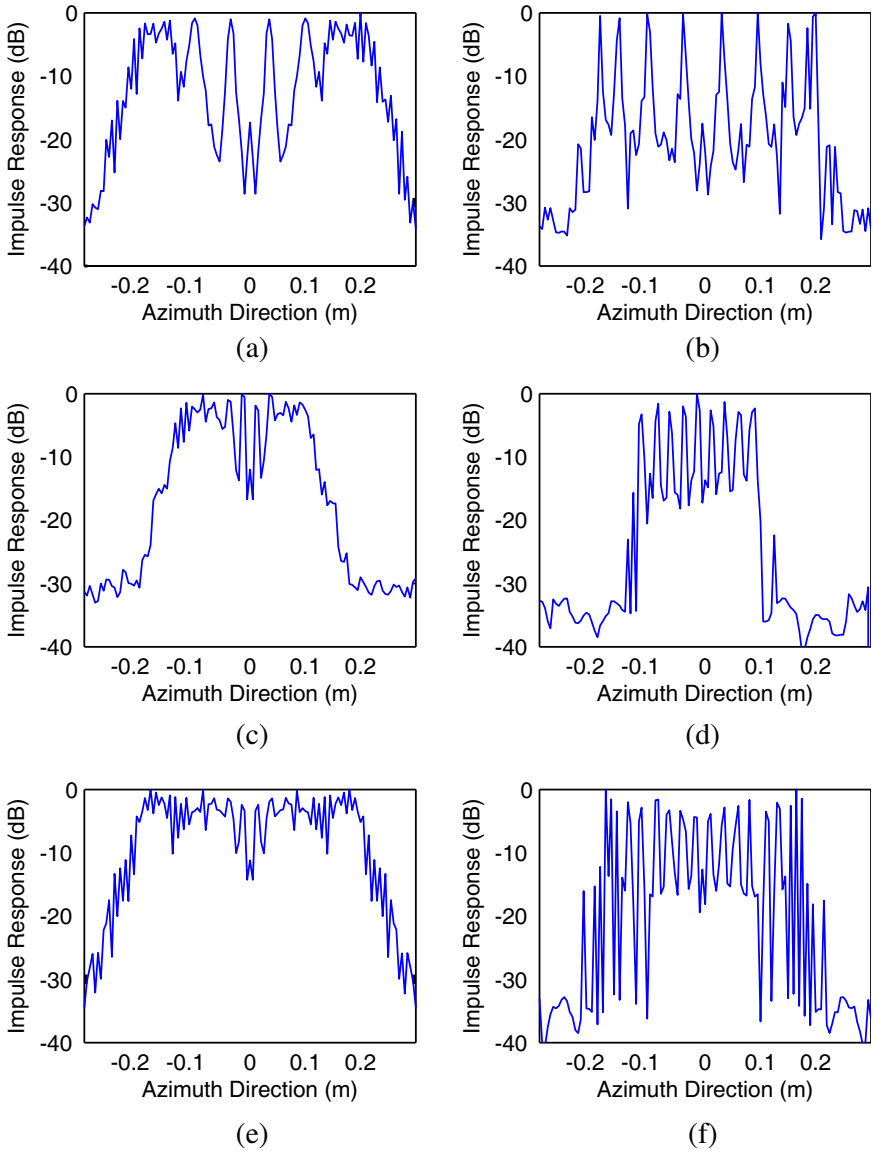

Figure 10. The profiles of the targets on the horizontal plane $z = 1.3911$ m directly projected onto the vertical plane, as in (a), (c) and (e), are improved and displayed in (b), (d) and (f) with the discussed method, respectively. The displayed dynamic range of the profiles is 40 dB.

Table 2. The measured PSLR, ISLR and resolutions in the ρ-axis, ϕ-axis and z-axis.

Measured Parameter	Azimuth	Polar-radius	Elevation
PSLR (dB)	−14.019	−17.712	−13.084
ISLR (dB)	−10.385	−17.498	−10.349
Resolution (cm)	0.591	2.512	0.674

PSF in the horizontal plane spreads in azimuth in Fig. 9(a) but not concentrates in polar-radius in Fig. 9(b). Hence, the PSLR and ISLR in polar-radius in Table 2 show a deviation from above typical values. But they do not produce any effect on the final image quality. From the point view of the indicators in Table 2, experimental results show a good performance in terms of focusing capabilities.

To demonstrate the validity of our approach for image display, we compare Fig. 4(c) and Figs. 7(b)–(c) with Fig. 4(g) and Figs. 7(e)–(f) at $z = 1.3911$ m, respectively. The directly projected images are shown in Figs. 10(a), (c), (e). Because of the worse resolutions in polar-radius and the shift-varying properties of PSF, the directly projected images are not very well. With the above approach the side lobes of the targets in polar-radius are decreased by greater than 10 dB, and the targets in the projected images can be easily separated, as shown in Figs. 10(b), (d), (f). Therefore, the method of image display can be used to improve the quality of the resulting images obtained within a cylindrical scanning geometry.

4. CONCLUSION

This paper presents a 3D imaging algorithm especially tailored for accurately reconstructing the 3D image of the human body in the case of cylindrical scanning geometry. The algorithm takes into account the free space propagation losses, the wavefront curvature and the case that the backscattering is not strictly isotropic within 360° by adjusting extent of ϕ_A. The core of the algorithm is the multiplication with the cylinder focusing function, followed by the coherent summation over the measured frequency ranges instead of the 3D frequency interpolation. In addition, the algorithm has the merit of parallel implementation without suffering from any approximations and the truncation errors. Furthermore, the sampling criteria and the resolutions for cylindrical configuration are deduced in detail. Finally, two numerical simulations are performed and the approach for better display of 3D image is presented. The measured indicators

of resulting images confirm the accuracy of the proposed algorithm with the cylindrical synthetic aperture for human body imaging.

ACKNOWLEDGMENT

The authors would like to thank the anonymous reviewers for providing a number of important comments and suggestions. This work is supported in part by the National Science Fund for Distinguished Young Scholars (Grant No. 60725103), the National Natural Science Foundation of China (Grant No. 60890070), the National Natural Science Foundation for Young Scientists of China (Grant No. 61002038) and by the Foundation (Grant No. A1320070058).

APPENDIX A. SOLUTION OF THE INTEGRAL USING FOURIER TRANSFORM

Fourier transforms are for converting a function between space and spatial frequency domains. Here, the 3D microwave reflectivity map associated with a person can be obtained using Fourier Transform.

Recall the expression for the response measured at transceiver position (ρ_0', ϕ', z') in (4)

$$E_R\left(K_\omega, \phi', z'\right) = \int\int\int_{\mathbf{V}} I\left(\rho, \phi, z\right) \exp\left(-j2K_\omega R\right) d\mathbf{r} \tag{A1}$$

Taking the Fourier transform of both sides in (A1) with respect to x', y' and z', we can write

$$\begin{aligned}
&\iiint_{\mathbf{V}'} E_R\left(K_\omega, \phi', z'\right) \exp\left(-jK_x x' - jK_y y' - jK_z z'\right) dx'dy'dz' \\
&= \iiint_{\mathbf{V}'} \left\{ \iiint_{\mathbf{V}} I\left(x, y, z\right) \exp\left(-j2K_\omega R\right) d\mathbf{r} \right\} \\
&\quad \times \exp\left(-jK_x x' - jK_y y' - jK_z z'\right) dx'dy'dz' \\
&= \iiint_{\mathbf{V}} I\left(x, y, z\right) \left\{ \iiint_{\mathbf{V}'} \exp\left(-j2K_\omega R\right) \right. \\
&\qquad \left. \times \exp\left(-jK_x x' - jK_y y' - jK_z z'\right) dx'dy'dz' \right\} dxdydz \\
&= C1 \iiint_{\mathbf{V}} I\left(x, y, z\right) \exp\left[-j\left(K_x x + K_y y + K_z z\right)\right] dxdydz
\end{aligned} \tag{A2}$$

where $\mathbf{V}'$ denotes the cylindrical synthetic aperture. K_x, K_y and K_z are the Fourier-transform variables corresponding to x, y and z,

respectively. These three wavenumbers are related with the frequency wavenumber K_ω through the following equations:

$$K_x = K_r \cos(\phi) = K_r \frac{(x - x')}{r} \tag{A3}$$

$$K_y = K_r \sin(\phi) = K_r \frac{(y - y')}{r} \tag{A4}$$

$$K_z = \sqrt{4K_\omega^2 - K_r^2} \tag{A5}$$

$$K_r = \sqrt{K_x^2 + K_y^2} = \sqrt{4K_\omega^2 - K_z^2} \tag{A6}$$

$$r = \sqrt{(x - x')^2 + (y - y')^2} \tag{A7}$$

The triple integral in the right-hand side of (A2) represents a 3D Fourier transform of the 3D microwave reflectivity function $I(x, y, z)$. Therefore, an estimate of $I(x, y, z)$ can be obtained by using a 3D inverse Fourier transform; that is

$$\begin{aligned} I(x,y,z) &= \frac{1}{C1} \iiint_K \left\{ \iiint_{\mathbf{V}'} E_R(K_\omega, \phi', z') \right. \\ &\quad \left. \times \exp\left(-jK_x x' - jK_y y' - jK_z z'\right) dx' dy' dz' \right\} \\ &\quad \times \exp\left[j(K_x x + K_y y + K_z z) \right] dK_x dK_y dK_z \\ &= \frac{1}{C1} \int_{K_z} \int_\phi \int_{K_\omega} \left\{ \iiint_{\mathbf{V}'} E_R(K_\omega, \phi', z') \right. \\ &\quad \left. \times \exp\left(-jK_x x' - jK_y y' - jK_z z'\right) \rho' d\rho' d\phi' dz' \right\} \\ &\quad \times \exp\left[j(K_x x + K_y y + K_z z) \right] K_\omega dK_\omega d\phi dK_z \\ &= \frac{\rho_0'}{C1} \int_{K_z} \int_\phi \int_{K_\omega} \left\{ \iint_S E_R(K_\omega, \phi', z') \right. \\ &\quad \left. \times \exp\left(-jK_x x' - jK_y y' - jK_z z'\right) d\phi' dz' \right\} \\ &\quad \times \exp\left[j(K_x x + K_y y + K_z z) \right] K_\omega dK_\omega d\phi dK_z \end{aligned} \tag{A8}$$

After rearranging the components of the above integral, we obtain

$$\begin{aligned} &I(x,y,z) \\ &= \frac{\rho_0'}{C1} \int_{z'} \int_{\phi'} \int_{K_\omega} E_R(K_\omega, \phi', z') \left\{ \int_\phi \int_{K_z} \exp\left[jK_x (x - x') \right] \right. \\ &\quad \left. \times \exp\left[jK_y (y - y') + jK_z (z - z') \right] d\phi dK_z \right\} K_\omega dK_\omega d\phi' dz' \end{aligned} \tag{A9}$$

In order to simplify the evaluation in (A9), the integral inside { } is further derived by substituting (A3)–(A7) into above identity.

$$\begin{aligned}
&\int_{\phi}\int_{K_z} \exp\left[jK_x\left(x-x'\right)+jK_y\left(y-y'\right)+jK_z\left(z-z'\right)\right]d\phi dK_z \\
&= \int_{\phi}\int_{K_z} \exp\left[jK_r\cos\left(\phi\right)\left(x-x'\right)\right] \\
&\quad \times \exp\left[jK_r\sin\left(\phi\right)\left(y-y'\right)+jK_z\left(z-z'\right)\right]d\phi dK_z \\
&= \int_{\phi}\int_{K_z} \exp\left[jK_r r\cos\left(\phi\right)\frac{(x-x')}{r}\right] \\
&\quad \times \exp\left[+jK_r r\sin\left(\phi\right)\frac{(y-y')}{r}+jK_z\left(z-z'\right)\right]d\phi dK_z \\
&= \int_{\phi}\int_{K_z} \exp\left[jK_r r\cos^2\left(\phi\right)\right] \\
&\quad \times \exp\left[jK_r r\sin^2\left(\phi\right)+jK_z\left(z-z'\right)\right]d\phi dK_z \\
&= \Delta\phi\int_{K_z} \exp\left[jK_r r+jK_z\left(z-z'\right)\right]dK_z \\
&= \Delta\phi\int_{K_z} \exp\left[j\sqrt{4K_\omega^2-K_z^2}\sqrt{(x-x')^2+(y-y')^2}\right] \\
&\quad \times \exp\left[jK_z\left(z-z'\right)\right]dK_z
\end{aligned} \tag{A10}$$

This results in the expression

$$\begin{aligned}
&\int_{\phi}\int_{K_z} \exp\left[jK_x\left(x-x'\right)+jK_y\left(y-y'\right)+jK_z\left(z-z'\right)\right]d\phi dK_z \\
&= \Delta\phi\exp\left(j2K_\omega R\right)
\end{aligned} \tag{A11}$$

By substituting (A11) in (A9), the reconstruction for $I\left(x,y,z\right)$ takes the form

$$\begin{aligned}
&I\left(x,y,z\right) \\
&= \frac{\Delta\phi\rho_0'}{C1}\int_{z'}\int_{\phi'}\int_{K_\omega} E_R\left(K_\omega,\phi',z'\right)\exp\left(j2K_\omega R\right)K_\omega dK_\omega d\phi' dz'
\end{aligned} \tag{A12}$$

Since $C1$, ρ_0' and $\Delta\phi$ are constants and only are related to the size of cylindrical synthetic aperture, their contributions in the image reconstruction are negligible. Therefore, we can obtain the following

$$I\left(\rho,\phi,z\right)=\int_{z'}\int_{\phi'}\int_{K_\omega} E_R\left(K_\omega,\phi',z'\right)\exp\left(j2K_\omega R\right)K_\omega dK_\omega d\phi' dz' \tag{A13}$$

REFERENCES

1. Sheen, D. M., D. L. McMakin, and T. E. Hall, "Three-dimensional millimeter-wave imaging for concealed weapon detection," *IEEE Trans. on Geoscience and Remote Sensing*, Vol. 49, No. 9, 1581–1592, 2001.
2. Sheen, D. M., H. D. Collins, T. E. Hall, D. L. McMakin, R. P. Gribble, R. H. Severtsen, J. M. Prince, and L. D. Reid, "Real-time wideband holographic surveillance system," European Patent 0925517B1, 2001.
3. Sheen, D. M., D. L. McMakin, and T. E. Hall, "Near-field three-dimensional radar imaging techniques and applications," *Applied Optics*, Vol. 49, No. 19, E83–E93, 2010.
4. Manfred, H., B. Gunnar, and E. Helmut, "Millimetre wave near field SAR scanner for concealed weapon detection," *Proceedings of EUSAR 2008*, 151–154, Friedrichshafen, Germany, 2008.
5. Grokhotkov, I. N. and A. Kuznetsov, "A concept of microwave system for the inspection of people and luggage," *Proceedings of EUSAR 2008*, 155–159, Friedrichshafen, Germany, 2008.
6. Oka, S., H. Togo, N. Kukutsu, and T. Nagatsuma, "Latest trends in millimeter-wave imaging technology," *Progress In Electromagnetics Research Letters*, Vol. 1, 197–204, 2008.
7. Bjarnason, J. E., T. L. Chan, A. W. Lee, M. A. Celis, and E. R. Brown, "Millimeter-wave, terahertz, and mid-infrared transmission through common clothing," *Applied Physics Letters*, Vol. 85, No. 4, 197–204, 2004.
8. Stolt, R., "Migration by Fourier transform techniques," *Geophysics*, Vol. 43, No. 1, 23–48, 1978.
9. Cafforio, C., C. Prati, and F. Rocca, "SAR data focusing using seismic migration techniques," *IEEE Transactions on Aerospace and Electronic Systems*, Vol. 27, No. 2, 194–207, 1991.
10. Soumekh, M., *Synthetic Aperture Radar Signal Processing with Matlab Algorithms*, John Wiley & Son, 1999.
11. Fortuny, J. and J. M. López-Sánchez, "Extension of the 3-D range migration algorithm to cylindrical and spherical scanning geometries," *IEEE Trans. on Antennas and Propagation*, Vol. 49, No. 10, 1434–1444, 2001.
12. Chen, H. M., S. Lee, R. M. Rao, M. A. Slamani, and P. K. Varshney, "Imaging for concealed weapon detection: A tutorial overview of development in imaging sensors and processing," *IEEE Signal Processing Magazine*, Vol. 22, No. 2, 52–61, 2005.

13. Appleby, R. and H. Wallace, "Standoff detection of weapons and contraband in the 100 GHz to 1 THz region," *IEEE Transaction on Antennas and Propagation*, Vol. 55, No. 11, 2944–2956, 2007.
14. Bertl, S., A. Dallinger, and J. Detlefsen, "Broadband circular interferometric millimetre-wave isar for threat detection," *Advances in Radio Science*, Vol. 5, 147–151, 2007.
15. Bertl, S. and J. Detlefsen, "Effects of a reflecting background on the results of active MMW SAR-imaging of concealed objects," *Proceedings of EUSAR 2010*, 120–123, Eurogress, Aachen, 2010.
16. Cooper, K. B., R. J. Dengler, G. Chattopadhyay, E. Schlecht, J. Gill, A. Skalare, I. Mehdi, and P. H. Siegel, "A high-resolution imaging radar at 580 GHz," *IEEE Microwave Wireless Components Letter*, Vol. 18, No. 1, 64–66, 2008.
17. Cooper, K. B., R. J. Dengler, N. Llombart, A. Talukder, A. V. Panangadan, C. S. Peay, I. Mehdi, and P. H. Siegel, "Fast, high-resolution terahertz radar imaging at 25 meters," *Proceedings of SPIE 2010*, Vol. 7671, 76710Y, 1–8, Orlando, Florida, USA, 2010.
18. Pinchuk, R., C. Sklarczyk, A. Bulavinov, and M. Kröning, "Stand-off detection of suspicious concealed objects in centimeter- and millimetre-wave range using sampling phased array principle and sparse array," *Proceedings of EUSAR 2008*, 163–164, Friedrichshafen, Germany, 2008.
19. Gumbmann, F., P. Hue Tran, J. Weinzierl, and L. Schmidt, "3D SAR processing for a fast scanning millimetre-wave short range imaging system," *Proceedings of EUSAR 2008*, 147–150, Friedrichshafen, Germany, 2008.
20. Tan, W. X., "Study on theory and algorithms for three-dimensional synthetic aperture radar imaging," Ph.D. Thesis, Institute of Electronics, Chinese Academy of Sciences, 2009 (in Chinese).
21. Solimene, R., A. Brancaccio, R. Di Napoli, and R. Pierri, "3D sliced tomographic inverse scattering experimental results," *Progress In Electromagnetics Research*, Vol. 105, 1–13, 2010.
22. Qi, F., V. Tavakol, D. Schreurs, and B. Nauwelaers, "Limitations of approximations towards fourier optics for indoor active millimeter wave imaging systems," *Progress In Electromagnetics Research*, Vol. 109, 245–262, 2010.
23. Abubakar, A., P. M. van den Berg, and S. Y. Semenov, "Two- and three- dimensional algorithms for microwave imaging and inverse scattering," *Journal of Electromagnetism Waves and Applications*, Vol. 17, No. 2, 209–231, 2003.

24. Ravan, M., R. K. Amineh, and N. K. Nikolova, "Two-dimensional near-field microwave holography," *Inverse Problems*, Vol. 26, No. 5, 1–21, 2010.
25. Kanj, H. and M. Popović, "A novel ultra-compact broadband antenna for microwave breast tumor detection," *Progress In Electromagnetics Research*, Vol. 86, 169–198, 2008.
26. Yu, J., M. Yuan, and Q. H. Liu, "A wideband half oval patch antenna for breast imaging," *Progress In Electromagnetics Research*, Vol. 98, 1–13, 2009.
27. Yu, Y., Q. H. Liu, and Z. P. Nie, "A new efficient FDTD time-to-frequency-domain conversion algorithm," *Progress In Electromagnetics Research*, Vol. 92, 33–46, 2009.
28. Zhang, H., S. Y. Tan, and H. S. Tan, "A flanged parallel-plate waveguide probe for microwave imaging of tumors," *Progress In Electromagnetics Research*, Vol. 97, 45–60, 2009.
29. Gong, Y. and G. Wang, "Superficial tumor hyperthermia with flat left-handed metamaterial lens," *Progress In Electromagnetics Research*, Vol. 98, 389–405, 2009.